

Stellar and orbital characterization of three low mass M dwarf binary stars with dynamical spectroscopy from the Habitable Zone Planet Finder*

SUHANI SURANA ,^{1,2,3} CHAD F. BENDER ,¹ CALEB I. CAÑAS ,^{4,†} DANIEL M. KROLIKOWSKI ,¹ WILLIAM D. COCHRAN ,⁵ MARK EVERETT ,⁶ ARVIND F. GUPTA ,⁶ SHUBHAM KANODIA ,⁷ SUVRATH MAHADEVAN ,^{8,9} ANDREW MONSON ,¹⁰ JOE P. NINAN ,¹¹ LEONARDO A. PAREDES ,¹ PAUL ROBERTSON ,¹² ARPITA ROY ,¹³ CHRISTIAN SCHWAB ,¹⁴ AND GUDMUNDUR STEFANSSON ,¹⁵

¹ *Steward Observatory and Department of Astronomy, University of Arizona, 933 N. Cherry Avenue, Tucson, AZ 85721, USA*

² *Department of Physics, University of Arizona, 1118 E. 4th Street, Tucson, AZ 85721, USA*

³ *Department of Computer Science, University of Arizona, Tucson, AZ 85721, USA*

⁴ *NASA Goddard Space Flight Center, 8800 Greenbelt Road, Greenbelt, MD 20771, USA*

⁵ *McDonald Observatory and Center for Planetary Systems Habitability, The University of Texas, Austin TX 78712 USA.*

⁶ *U.S. National Science Foundation, National Optical-Infrared Astronomy Research Laboratory, 950 N. Cherry Ave., Tucson, AZ 85719, USA*

⁷ *Earth and Planets Laboratory, Carnegie Science, 5241 Broad Branch Road, NW, Washington, DC 20015, USA*

⁸ *Department of Astronomy & Astrophysics, 525 Davey Laboratory, 251 Pollock Road, Penn State, University Park, PA, 16802, USA*

⁹ *Center for Exoplanets and Habitable Worlds, 525 Davey Laboratory, 251 Pollock Road, Penn State, University Park, PA, 16802, USA*

¹⁰ *Steward Observatory and Department of Astronomy, University of Arizona, 933 N. Cherry Ave., Tucson, AZ 85721, USA*

¹¹ *Department of Astronomy and Astrophysics, Tata Institute of Fundamental Research, Homi Bhabha Road, Colaba, Mumbai 400005, India*

¹² *Department of Physics & Astronomy, University of California, Irvine, CA 92697, USA*

¹³ *Astrophysics & Space Institute, Schmidt Sciences, New York, NY 10011, USA*

¹⁴ *School of Mathematical and Physical Sciences, Macquarie University, Balaclava Road, North Ryde, NSW 2109, Australia*

¹⁵ *Anton Pannekoek Institute for Astronomy, 904 Science Park, University of Amsterdam, Amsterdam, 1098 XH*

ABSTRACT

Theoretical models of low-mass stars continue to be discrepant with observations when used to examine the mass-radius relationship and other physical parameters of individual stars. High-resolution spectroscopy that leads to dynamical measurements of binary stars can directly improve these models. We have been using the Habitable-zone Planet Finder spectrograph to monitor binary stars with M dwarf components. Here, we measure the orbital and stellar parameters for three such systems: LSPM J0515+5911, NLTT 43564, and NLTT 45468. Each system has dozens of spectra obtained over a baseline of several years. None of the systems appear to be eclipsing, so our ability to turn them into true benchmark binaries with purely dynamical measurements is limited. We use literature photometry to estimate each system's spectral energy distribution and utilize models in combination with detection limits of our spectroscopic measurements to probe characteristics of the companions. LSPM J0515+5911 is a double-lined spectroscopic binary with period of 126.948 ± 0.029 days and derived minimum masses, $M_1 \sin^3 i = 0.058 \pm 0.002 M_{\odot}$ and $M_2 \sin^3 i = 0.046 \pm 0.001 M_{\odot}$ for the primary and secondary components, respectively. We solved NLTT 43564 with period of 1877 ± 24 days and NLTT 45468 with period of 9.686 ± 0.001 days as single lined systems, and modeled the primary masses to be $M_1 = 0.32 \pm 0.02 M_{\odot}$ and $M_1 = 0.35^{+0.02}_{-0.07} M_{\odot}$, respectively.

suhanisurana@arizona.edu

cbender@arizona.edu

* Based on observations obtained with the Hobby-Eberly Telescope (HET), which is a joint project of the University of Texas at Austin, the Pennsylvania State University, Ludwig-Maximilians-Universitaet Muenchen, and Georg-August Universitaet Goettlingen. The HET is named in honor of its principal benefactors, William P. Hobby and Robert E. Eberly.

Keywords: Binary stars (154); Companion stars (291), Low mass stars (2050)

1. INTRODUCTION

A large fraction of the star systems in our galaxy contain multiple stellar components (Duquennoy & Mayor 1991; Raghavan et al. 2010). Binary stars are empirical probes for theoretical models of star formation and evolution, and underpin much of our understanding of stellar astrophysics. M dwarfs make up the majority of stars in the solar neighborhood (Henry et al. 2006, 2018), but have been difficult to observe due to their small size and intrinsically low luminosity. As a result of limited observations and the complexity of their structure and evolution, late M dwarfs (e.g., Spada et al. 2013; Maxted et al. 2023), are less well understood than Sun-like (FGK) stars. Directed observations of M dwarfs, when combined with stellar models, can broaden our understanding of these low-mass stellar populations. They are also promising targets for exoplanet searches due to their low luminosities, which place the habitable zone closer to the star than around Sun-like stars. This results in shorter orbital periods and more favorable signals (e.g., contrast ratios, semi-amplitude velocities) that are easier to observe than for analogous planets around Sun-like stars. The proximity of the habitable zone facilitates atmospheric characterization, with current or upcoming instruments, such as the James Webb Space Telescope (Gialluca et al. 2021), ground-based Extremely Large Telescopes (Hardegree-Ullman et al. 2023), and the future Habitable Worlds Observatory (Tuchow et al. 2024). Characterizing such systems, however, requires well-constrained stellar and orbital parameters (e.g., Kopparapu et al. 2013, 2017; Shields et al. 2016). Model isochrones are not well-constrained for M dwarfs because of the relative dearth of empirical M dwarf masses (Parsons et al. 2018).

Double-lined spectroscopic binaries provide dynamical mass measurements that are mostly model independent. Measurements from these star systems help refine and improve models of stellar structure (Maxted et al. 2023). In this paper, we present precision spectroscopic measurements for three systems: LSPM 0515+5911 whose primary star has a spectral type of M7.0V (Lépine et al. 2003); NLTT 43564 (LSPM J1645+6057) whose primary star has a spectral type of M3.5V (Alonso-Floriano et al. 2015) and NLTT 45468 (LSPM J1746+6024) whose primary star has a spectral type of M4.5 (Reid et al. 2004).

Table 1 provides a summary of literature values for these systems.

We started observing these and other M dwarf targets in 2019 with the Habitable-zone Planet Finder (HPF) spectrograph (Mahadevan et al. 2012), as part of a Guaranteed Time Observation program designed to search for exoplanets around M dwarfs. This program has produced numerous planet discoveries and followup confirmations (e.g., Lubin et al. 2021; Stefánsson et al. 2023; Beard et al. 2025). We quickly identified these targets as spectroscopic binaries based on large orbital motion in the primary velocities, and because of their low stellar masses we continued observing them at a low cadence over the subsequent years. We used our HPF spectra to measure the radial velocities of individual binary components, derived orbital parameters for each system, and combined these with photometry from the Gaia (Gaia Collaboration et al. 2018, 2023), Pan-STARRS (Chambers et al. 2016), APASS (Henden et al. 2015), and 2MASS (Lépine et al. 2003) surveys to estimate the physical parameters for individual stellar components. We also utilized high contrast and high resolution measurements from the speckle imagers NESSI and 'Alopeke (Scott et al. 2018; Scott & Howell 2018), and imaging from Robo-AO (Riddle et al. 2012), to look for potential contamination from background sources.

In §2, we describe the facilities and data products used for this work. In §3 we discuss the detailed analysis of the data, including extracting radial velocities (RVs), data analysis and modeling methods, and the determination of stellar parameters. In §4 we describe the three binary stars that have been analyzed, provide some discussion of the systems. In §5 we conclude by summarizing the work discussed and provide remarks about the future of this HPF binary star program.

2. OBSERVATIONS

2.1. High-resolution spectroscopy with HPF

The spectroscopic observations listed in Table 2 were all obtained with HPF (Mahadevan et al. 2012), on the 10 m Hobby Eberly Telescope (HET) (Ramsey et al. 1998; Ramsey 2005; Hill et al. 2021), at McDonald Observatory, Texas. HPF is a high-resolution ($R \sim 53,000$), 1.7" fiber-fed (Kanodia et al. 2018), temperature controlled (Stefánsson et al. 2016), near-infrared ($\lambda \sim 8,080 - 12,780 \text{ \AA}$) spectrograph. HPF uses gold-coated mirrors, a mosaic echelle grating, and a single

[†] NASA Postdoctoral Program Fellow

Table 1. Primary Star Parameters.

Parameter	LSPM J0515+5911	NLTT 45468	NLTT 43564
Primary Star Parameters			
Gaia DR3	281261607033049472	1435275923117125760	1624385699685942912
TIC ID	87302025	219807052	289536553
RA (HH:MM:SS)	05:15:30.95	17:46:11.64	16:45:55.05
Dec (DD:MM:SS)	+59:11:17.44	+60:24:26.22	+60:57:03.96
Proper motion (RA) (mas yr ⁻¹)	116.467 ± 0.211	-79.414 ± 0.021	22.24 ± 0.30
Proper motion (DEC) (mas yr ⁻¹)	-1005.994 ± 0.182	214.516 ± 0.0170	-279.60 ± 0.30
Parallax (mas)	63.36 ± 0.24	35.57 ± 0.01	46.68 ± 0.09
RUWE	4.631	1.235	17.164
Photometry			
Pan-STARRS <i>g</i> ^b	18.687 ± 0.016 ^a	15.465 ± 0.021	...
Pan-STARRS <i>r</i> ^b	17.311 ± 0.012 ^a	14.199 ± 0.005	...
Pan-STARRS <i>i</i> ^b	14.661 ± 0.002 ^a	12.730 ± 0.120	...
Pan-STARRS <i>z</i> ^b	13.593 ± 0.017 ^a
Pan-STARRS <i>y</i> ^b	12.868 ± 0.004 ^a	11.504 ± 0.045	...
Gaia <i>BP</i> ^c	18.335 ± 0.013 ^a	15.0819 ± 0.0037	13.7076 ± 0.0030 ^a
Gaia <i>RP</i> ^c	13.8142 ± 0.0011 ^a	12.0067 ± 0.0013	11.0165 ± 0.0013 ^a
Gaia <i>G</i> ^c	15.2895 ± 0.0007 ^a	13.2902 ± 0.0005	12.2114 ± 0.0008 ^a
APASS <i>B</i> ^d	...	16.638 ± 0.204 ^a	14.973 ± 0.124
APASS <i>V</i> ^d	...	14.702 ± 0.067 ^a	13.411 ± 0.036
APASS <i>g</i> ^d	...	15.608 ± 0.170 ^a	14.204 ± 0.049
APASS <i>r</i> ^d	...	14.106 ± 0.027 ^a	12.855 ± 0.040
APASS <i>i</i> ^d	...	12.298 ± 0.164 ^a	11.382 ± 0.032
2MASS <i>J</i> ^e	11.320 ± 0.025	10.011 ± 0.027 ^a	9.393 ± 0.026
2MASS <i>H</i> ^e	10.661 ± 0.019	9.372 ± 0.024 ^a	8.840 ± 0.027
2MASS <i>K_s</i> ^e	10.319 ± 0.018	9.039 ± 0.018 ^a	8.568 ± 0.025
WISE 1 ^f	10.001 ± 0.023
WISE 2 ^f	9.792 ± 0.020
WISE 3 ^f	9.440 ± 0.040
WISE 4 ^f	9.023 ± 0.464

^aNot used in the SED Fit described in §3.2

References— ^b Pan-STARRS: (Chambers et al. 2016); ^c Gaia DR2: (Gaia Collaboration et al. 2018), Gaia DR3: (Gaia Collaboration et al. 2023); ^d APASS: (Henden et al. 2015); ^e 2MASS: (Cutri et al. 2003); ^f WISE: (Cutri et al. 2021)

Teledyne Hawaii-2RG (H2RG) NIR detector with a 1.7-micron cutoff covering parts of the z, Y and J NIR bands (Mahadevan et al. 2014). HPF observations are queued and executed by the resident astronomers at the HET (Shetrone et al. 2007). This allows us to target observations of binary stars at specific orbital phases and facilitates long-term observing programs needing measurements on monthly or every few months cadence.

We executed observations at strategic orbital phases to cover the full binary orbits of our target systems with

a signal-to-noise ratio (S/N) sufficient to probe for a signal from the secondary star. HPF operations impose a maximum single exposure time of 945 seconds. As this program progressed, we adapted the requested exposure time of each target to adjust the S/N, and to stay within time allocated for the program. In some cases, Table 2 lists back-to-back exposures on a single night; this represents exposure sequences structured to keep under the maximum individual exposure time, and which we subsequently analyzed independently. In May

2022, HPF required maintenance that included a vacuum cycle, which resulted in two RV eras, the “pre” and “post”, corresponding to RVs before and after this cycle. There is a small offset in the RVs at the m s^{-1} level observed across these eras. In the analysis in §3, we treat RVs from these eras as coming from two different instruments.

All spectra were extracted using the standard HPF pipeline which uses the `HxRGproc` code¹ which processes the data and performs bias noise removal, nonlinearity correction, cosmic-ray correction, and slope/flux and variance image calculation (Ninan et al. 2019). Observations in the pre era were extracted using a classical optical extraction, which automatically removes the signature of the echelle blaze. In the post era, the extraction changed to a flat-relative algorithm, and the blaze was manually removed based on a static correction obtained by sum extracting very high S/N continuum lamp spectra and smoothing them to remove detector pixel QE variations. This pipeline change was implemented because of a software upgrade to the computer cluster that runs the pipeline, which made utilizing the original code difficult. The updated pipeline produces functionally identical extracted spectra to the old pipeline.

Standard HPF operations obtain Laser-Frequency Comb (LFC) wavelength calibration observations throughout the night (Metcalf et al. 2019), and the pipeline interpolates these to derive the wavelength solution at the time of any specific science observations (Stefansson et al. 2020). §2.1.1 describes our procedure for correcting telluric absorption. We computed barycentric corrections using `barycorrpy`² (Kanodia & Wright 2018) based on algorithms presented in Wright & Eastman (2014).

LSPM 0515+5911 was observed on 24 epochs from 2020 January to 2022 February. NLTT 43564 was observed on 73 epochs from 2019 April to 2025 April. NLTT 45468 was observed on 80 epochs from 2019 May to 2025 June. The median per-pixel S/N in HPF order index 18 ($\lambda \sim 10,700 \text{ \AA}$, approximately the center of HPF’s bandpass, where the HPF exposure time calculator works), RVs of all HPF observations, and 1σ uncertainties are reported in Table 2. For NLTT 45468, the median per-pixel S/N is 39.6 in HPF order index 1 (8079–8184 \AA) and 91.8 in the HPF order index 28 (12625–12786 \AA).

2.1.1. Telluric Correction

The Earth’s atmosphere absorbs broad swaths of light across the near-infrared bandpass of HPF. To correct this telluric contamination, we apply a method that combines a suite of model atmospheric transmission spectra with a model of the HPF instrumental line spread function (LSF). This paper is the first to use the HPF data processed with this telluric correction algorithm. An accurate LSF model is required to convolve with the transmission model spectra to reflect the telluric contamination as observed in HPF spectra. Below we provide a brief description of our procedure and defer a more detailed discussion of the HPF LSF model and telluric correction to a future paper focused on the method (Krolikowski et al. in prep³).

To prepare for the telluric correction, we first fit a model of the HPF instrumental LSF to LFC spectra (Metcalf et al. 2019). The LFC provides emission lines across the entire HPF bandpass with extremely narrow intrinsic width, meaning that the observed LFC line profile is nearly the instrumental LSF. The model is parameterized as a Gaussian convolved with a trapezoid multiplied by an orthogonal polynomial, with the latter two elements accounting for non-Gaussianity and asymmetry. The resulting LSF model can be evaluated at any given point in an HPF spectrum. We then generate a grid of model transmission spectra for species that absorb within the HPF bandpass (H_2O , O_2 , CO_2 , and CH_4) over a range of water vapor column and zenith angle values. We generate the transmission spectra using line-by-line radiative transfer modeling (LNFLv3.2 and LBLRTM12.15.1, Clough et al. 1992, 2005) and the molecular line lists from AER and HITRAN (AER 2020; Gordon et al. 2022). We use the default O_2 LBLRTM abundance, fix the CO_2 abundance to 420 ppm, and fix the CH_4 abundance to 1860 ppb (roughly the average atmospheric concentrations during the observation epochs presented here). Most of the telluric absorption in HPF band is H_2O and O_2 , so CO_2 and CH_4 are not critical.

To generate a telluric model for each observation, we first interpolate the model transmission spectra grid to the observation’s zenith angle. We then convolve the model grid using the HPF LSF model and fit for the water vapor column using select wavelength regions where we expect minimal contamination from stellar spectral lines. Lastly, we combine the model transmission spectra for each molecular species to generate a full telluric line absorption model across the entire HPF spectrum.

¹ <https://github.com/indiajoe/HxRGproc>

² <https://github.com/shbhuk/barycorrpy>

³ An in-progress version of the code to generate the telluric model can be found at https://github.com/dkrolikowski/eprv_telluric_correction

Table 2. HPF Spectroscopy Epochs and Radial Velocity Measurements

UT Date	BJD _{TDB} -2,400,000	V_A (km s ⁻¹)	σ_A (km s ⁻¹)	V_B (km s ⁻¹)	σ_B (km s ⁻¹)	S/N ^a
LSPM J0515 + 5911 – 24 epochs						
2020 Jan 10	58858.631101	-49.220	0.061	39.7
2020 Jan 10	58858.642743	-49.164	0.062	38.5
2020 Jan 31	58879.730610	-45.966	0.063	-57.056	0.587	64.2
2020 Jan 31	58879.742138	-45.984	0.062	-56.942	0.607	62.7
2020 Feb 04	58883.699353	-45.935	0.064	-57.208	0.592	42.5
2020 Feb 04	58883.710931	-45.914	0.064	-56.558	0.767	50.5
2020 Sep 02	59094.956441	-67.219	0.058	-29.036	0.478	40.9
2020 Sep 30	59122.888262	-46.593	0.059	-55.817	0.947	55.7
2020 Nov 05	59158.958795	-46.699	0.057	-55.220	1.326	70.4
2020 Nov 05	59158.970129	-46.674	0.058	-55.783	0.665	71.1
NLTT 43564 – 73 epochs						
2019 Apr 19	58592.839000	-32.872	0.061	160.8
2019 Apr 19	58592.850000	-32.844	0.061	181.4
2020 Feb 17	58896.997000	-32.633	0.061	121.4
2020 Feb 17	58897.010000	-32.637	0.067	70.0
2020 Mar 11	58919.934000	-32.623	0.058	132.2
2020 Mar 11	58919.946000	-32.646	0.059	132.3
2020 Apr 14	58953.849000	-32.573	0.062	92.9
2020 Apr 14	58953.860000	-32.633	0.061	102.9
2020 Apr 21	58960.971000	-32.605	0.056	195.0
2020 Apr 21	58960.982000	-32.594	0.055	202.2
NLTT 45468 – 80 epochs						
2019 May 24	58627.774000	-12.083	0.070	107.5
2019 May 24	58627.786000	-12.115	0.069	106.1
2019 Sep 04	58730.665000	-12.061	0.067	109.4
2019 Sep 04	58730.677000	-12.069	0.065	115.9
2019 Sep 16	58742.594000	-12.100	0.079	59.4
2019 Sep 16	58742.607000	-12.185	0.085	53.7
2019 Sep 18	58744.633000	-12.016	0.069	93.3
2019 Sep 18	58744.645000	-12.030	0.070	89.1
2020 Feb 27	58906.996000	-12.239	0.083	56.6
2020 Feb 27	58907.008000	-12.234	0.079	62.2

NOTE—This table is published in its entirety in the machine-readable format. A portion is shown here for guidance regarding its form and content.

^aThe S/N is calculated as the median of flux/ $\sqrt{\text{variance}}$ in order index 18, near 10,700 Å, which is the peak of the HPF throughput.

We corrected for telluric lines in the target spectrum by dividing the science flux by the telluric line absorption model, which although not strictly mathematically correct, is accurate to within a few percent which although not strictly mathematically correct, is accurate to a few tenths of a percent for most lines and better than 2% for the deepest lines (eg., Latouf et al. 2022, Fig 5).

2.2. High-contrast imaging with ground based instruments

We used high-contrast imaging to search for any bright stars near our targets that could contaminate spectra obtained with HPF's 1.7" fiber. Common false positive scenarios that might affect our analysis include blended and/or unresolved background binaries, where the light from additional stars within the aperture contaminates the signal in our spectrograph; Fleming et al. (2015) describe the full suite of contamination possibilities. We observed each of our targets with the NN-Explore Exoplanet Stellar Speckle Imager (NESSI; Scott et al. 2018) on the 3.5 m WIYN Telescope at the Kitt Peak National Observatory (Scott et al. 2018). We also inspected archival data from 'Alopeke speckle imaging (Scott et al. 2018; Howell et al. 2011) and Robo-AO adaptive optics (Riddle et al. 2012; Lamman et al. 2020) imaging for NLTT 43464.

2.2.1. NESSI Speckle Imaging

We obtained speckle observations of LSPM 0515+5911 on 2022 April 21, NLTT 43564 on 2022 April 17, and NLTT 45468 on 2022 April 17 using NESSI (PI: Gupta, 2022A-665981). We processed the data using the reduction procedures described in Howell et al. (2011). A 9 minute sequence with 40 ms exposure times was obtained using NESSI's red camera, capturing diffraction limited speckle images in the Sloan z' filter. Figure 1a, 1b, and 1c show the contrast curves for NLTT 43564, NLTT 45468 and LSPM J0515 + 5911, respectively. For NLTT 43564, there are no nearby sources brighter than $\Delta z' = 4.45$ at separations greater than 0''.5. For NLTT 45468, a companion is visible at $\approx 2''.056$ with delta mag of 1.91 in SDSS z' filter, that for HPF likely results in blending and causes observed distortions in the differential line width (see §4.2). This companion was identified by Gaia (Gaia DR3 1435275918821040000) and we discuss it further in §4.2. For LSPM J0515 + 5911, there is no evidence of bright companions or significant flux contamination brighter than $\Delta z' = 4.45$ between 0.2" – 1.2" from the target.

2.2.2. Adaptive optics imaging with Robo-AO

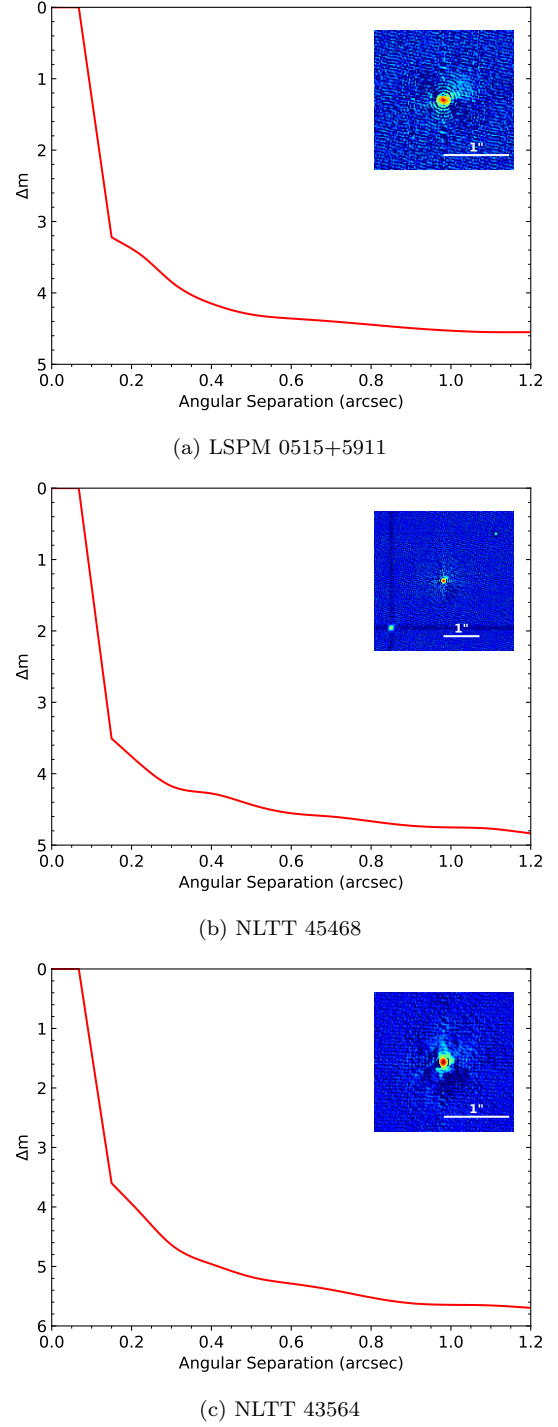


Figure 1. Contrast curves and reconstructed images from the NESSI speckle imager for *a*: LSPM 0515+5911, *b*: NLTT 45468, and *c*: NLTT 43564. Neither LSPM 0515+5911 nor NLTT 43564 show companions within the field that could contaminate the HPF observations. NLTT 45468 shows a nearby star at 2.1" in the lower left of the inset in *b*; the signal in the upper right is an artifact of the speckle processing.

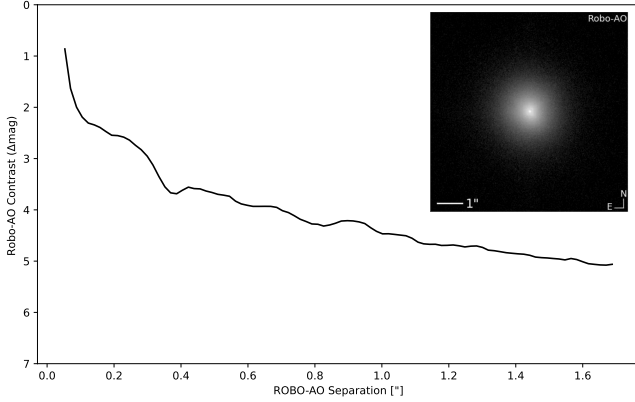


Figure 2. Robo-AO contrast curves for NLTT 43564 obtained with the Robo-AO laser Adaptive Optics system. The curves show the 5σ detection limits (Δm) as a function of angular separation. The inset of $1'' \times 1''$ shows the reconstructed speckle image at 832 nm. No nearby companions are detected within $1.6''$ angular separation of the target.

The Robo-AO laser Adaptive Optics system on the 2.1 m telescope at Kitt Peak National observatory observed NLTT 43564 on 17th April 2017 as part of a survey of M dwarf multiplicity (Lamman et al. 2020). The data are available through the Exoplanet Follow-up Observation Program (Christiansen et al. 2025; NExSci 2022). The data were reduced with the Robo-AO pipeline (Law et al. 2014), which performs PSF subtraction, searches for stellar companions, and computes 5σ contrast curves to estimate detection limits. Ziegler et al. (2018) presents a detailed description of the data reduction pipeline. Figure 2 shows the Robo-AO contrast curve for NLTT 43564: there are no close companions within $1''$ of separation.

2.2.3. 'Alopeke speckle imaging

NLTT 43564 was observed by the 'Alopeke Speckle Imager on the Gemini North telescope on 24th June 2021 (GN-2021A-Q-312, PI: Jao, NExSci (2022)) to search for any nearby close companions (Scott et al. 2018; Howell et al. 2011). 'Alopeke has simultaneous dual channel imaging at 562 nm ($\Delta\lambda = 54$ nm) and 832 nm ($\Delta\lambda = 40$ nm). It has a pixel scale of $0''.01$ pixel $^{-1}$ and a diffraction limited PSF of $\approx 0''.02$. Figure 3 shows the contrast curve along with the inset at 832 nm. No bright companions are evident within $1''.2$, with detection limits of $\Delta m \approx 3.5$ at $0''.18$ and $\Delta m \approx 7.5$ at $1''$ in the 832 nm band, consistent with the single point source.

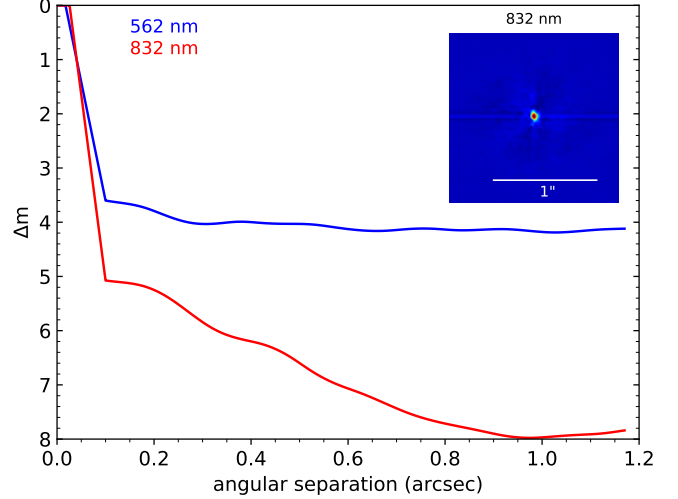


Figure 3. Speckle imaging contrast curves for NLTT 43564 (GAI 1645+6057) obtained with the 'Alopeke Speckle Imaging at Gemini at 562 nm (blue) and 832 nm (red). The curves show the 5σ detection limits (Δm) as a function of angular separation. The inset of $1'' \times 1''$ shows the reconstructed speckle image at 832 nm. No nearby companions are detected within $1.2''$ angular separation of the target.

3. DATA ANALYSIS

3.1. Analysis of Single Line and Double Line Spectroscopic Binaries

We used the TODCOR algorithm (Mazeh & Zucker 1992) to measure the radial velocities of the individual stars in our HPF spectra. TODCOR performs a two-dimensional (2D) cross correlation between the observed spectrum and two theoretical or observed templates shifted by different velocities. TODCOR is an efficient algorithm that uses the Fast Fourier Transform to compute cross correlations in multiple dimensions, solving for v_1 and v_2 , the radial velocities for the primary and secondary star, and α , the flux ratio between the two stars. TODCOR computes the two-dimensional correlation function over a grid of velocity pairs with uniform spacing in velocity, and identifies the combination of v_1 , v_2 , and α that maximizes the correlation. This approach can, given sufficient S/N in the observations, disentangle blended spectral features at velocities near the systemic velocity, that would otherwise introduce a bias in a one-dimensional (1D) correlation.

We estimated the uncertainties of the primary and secondary velocity measurements as a combination of the intrinsic velocity uncertainty of the templates and the uncertainty in measuring the center of the correlation peak due to its intrinsic width, as measured by fitting a quadratic polynomial fit to the correlation peak (see Bender & Simon 2008, for more details). We used an IDL based version of TODCOR, SXCORR (Bender & Si

mon 2008; Bender et al. 2012), which implements a convenient interface to interactively explore the correlation space in complicated systems, allows for both one- and two-dimensional cross-correlations, and has an option to lock α to a known fixed value.

Our analysis started with a standard 1D cross correlation to quickly estimate the velocities of the primary star, and place bounds on the stellar parameters of the template and the plausible velocity parameter space of the secondary star. We then use those bounds to conduct a more focused 2D analysis with the full TOD-COR algorithm. The stellar parameters of the template, such as spectral type, temperature, surface gravity, metallicity, and rotational velocity, are indicative of the underlying spectral type of the star. However, slight mismatches in the template parameters, have only a minimal impact on the measured RVs in a 1D correlation, and mostly manifest as a change in correlation amplitude. Therefore, we use the maximum correlation value as an indicator of the best matching template. We use the maximum-likelihood method presented in Zucker (2003) to combine multiple contiguous regions of spectra, which are separated by order gaps and by areas of uncorrectable telluric absorption. This algorithm is unable to correctly account for changes in α with wavelength that naturally occur with spectra spanning a wide bandpass, so in that event we follow the procedure outlined in Bender et al. (2012) to combine spectral regions with varying α .

For the SB2 target LSPMJ0515 + 5911, we measured a range of α for the epochs with well-separated peaks in the cross-correlation function, and then locked it for the epochs where the peaks are blended. We used ten spectra with cleanly separated peaks to constrain alpha from 0.17 to 0.20, and then locked α to 0.18, as was done in Bender et al. (2012); variations within this range result in negligible variation in the measured RVs. Mismatches between the stellar parameter of the template and observed spectra can significantly impact the estimate of α . But for cool M dwarfs, where spectra at HPF's resolution are comprised of numerous blended lines, including molecular features, the measured RVs are stable over small variations in template parameters, while the correlation amplitude can be highly variable. In binaries with low α , where the primary star's light is dominant (i.e., α of a few percent), the RVs are tolerant to changes in α of a factor of two to three. For each system, we initially characterized the orbital parameters by fitting the RVs in Table 2 using a Levenberg-Marquardt optimization algorithm to solve Kepler's 2nd law. This approach constrained ω and e , and allowed us to derive initial values for the orbital parameters by minimizing the chi-squared

metric. This optimization was then used to inform the priors used in a MCMC optimization for each system, which are listed in Table 3. The `exoplanet`⁴ (Foreman-Mackey et al. 2021) modeling toolkit was developed for the analysis of exoplanets, but since the underlying orbital physics is the same, we used it for spectroscopic binaries. `exoplanet` implements a Hamiltonian Monte Carlo (HMC) parameter estimation from PyMC3 (Salvatier et al. 2015) using the Gelman-Rubin statistic of $\hat{R} < 1.1$ (Ford 2006) to check for convergence.

In `exoplanet`, we create a probabilistic model in PyMC3 to fit the RV curves, which consist of 8 independent parameters for an SB1 and 9 for an SB2, including the orbital period P , the time of inferior conjunction T_0 , $\sqrt{e} \cos \omega$, $\sqrt{e} \sin \omega$ where e is eccentricity e and ω is the argument of the periaxis of the star's orbit, semi-amplitude K_1 , K_2 (for SB2s only), a jitter term that includes stellar and instrument RV jitter, σ_{HPF} , and the systemic velocity, γ .

After providing initial priors for the six orbital parameters, we modeled the RVs using a standard Keplerian model. To account for pre/post era RV measurements we used two different radial velocity jitters, $\sigma_{HPF_{pre}}$ and $\sigma_{HPF_{post}}$, and two offset parameters γ_{pre} and γ_{post} , that are treated independently. The jitter term is added in quadrature to the observed RV uncertainties when calculating the likelihood function. The derived parameters, along with their uncertainties, are given in Table 3.

3.2. Determination of Stellar Parameters

To estimate the stellar parameters of the primary star, we utilized HPF-SpecMatch⁵ (Stefansson et al. 2020) which is broadly based on the algorithms described in Yee et al. (2017). In HPF-SpecMatch, the spectrum is deblazed, sky corrected, barycentric corrected and then is interpolated to a grid of wavelengths spanning $\lambda \sim 8656 - 8768\text{\AA}$ due to minimal telluric contamination in that region. Then, for each star, the spectrum is rotationally broadened by a projected rotational velocity and multiplied by a Chebyshev polynomial to remove any low-order residual variations in the corrected spectra. HPF-SpecMatch first identifies the best-fit between the target spectrum and each library spectrum and then provides the five best matched templates. It then linearly combines the five spectra into a single composite spectrum and derives stellar parameters T_{eff} , $[Fe/H]$, $\log g$ and $v \sin i$ for the primary star as the weighted average of the five best match library stars. To

⁴ <https://github.com/exoplanet-dev/exoplanet>

⁵ <https://github.com/gummiks/hpfspecmatch>

obtain the spectroscopic parameters for SB1s, we ran **HPF-SpecMatch** on the highest S/N visit for each system, while for the SB2, we chose the epoch for a point at RV gamma, when the separation between the primary/secondary is ~ 0 km/s. The results are given in Table 3. We have intentionally excluded $v \sin i$, because we believe the significance of the values derived for it by **HPF-SpecMatch** to be low. To derive the model dependent stellar parameters for the primary star, we used **astroARIADNE**⁶ (henceforth, **Ariadne**; Vines & Jenkins 2022) software which is a spectral energy distribution (SED) Bayesian model averaging fitter. **Ariadne** models the available broadband photometry, which is provided in Table 1. The SED fit adopts Gaussian priors on (i) broadband photometry listed in Table 1; (ii) the spectroscopic constraints on $\log g$, T_{eff} , and $[Fe/H]$ obtained from our **HPF-SpecMatch** analysis; (iii) Gaia DR3 parallax and (iv) Bailer-Jones distance (Bailer-Jones et al. 2021). **Ariadne** also applies an upper bound on the visual extinction using the SFD dust maps (defined in Schlegel et al. 1998) from Schlafly & Finkbeiner (2011), evaluated at the Bailer-Jones distance and converted to AV with the Fitzpatrick (1999) reddening law assuming $R_V = 3.1$. Table 1 summarizes the full set of literature photometry used in the joint analysis, and Table 3 lists the stellar parameters inferred from **HPF-SpecMatch** along with their uncertainties.

4. RESULTS AND DISCUSSION

4.1. LSPM J0515+5911

LSPM J0515+5911 consists of a primary M7 star in a binary system with a companion on a 126.948 ± 0.029 day eccentric orbit. We solved this system as a double-lined spectroscopic binary. We used **HPF-Specmatch** to derive the stellar parameters based on a single high-S/N HPF observation that we obtained very close to the systemic velocity, and which yielded values of $T_{\text{eff}} = 2875 \pm 59$ K, $\log g = 5.17 \pm 0.04$, $[Fe/H] = -0.02 \pm 0.16$, $v \sin i = 1 \pm 18$ km s $^{-1}$. This corresponds to a primary template constructed from a spectrum of the star LSPM J0011+5908. We used observations obtained near quadrature to optimize the secondary template, by maximizing the correlation value, constructed from an HPF spectrum of the star GJ 644 C. We measured the primary velocity in 24 HPF spectra, and the secondary velocity in 16 of those spectra. The 8 spectra where we did not recover the secondary have low S/N or substantial blending be-

tween the two stars in velocity space. Figure 4 shows the primary and secondary RVs and corresponding orbital fits. The eccentricity is $e = 0.571 \pm 0.002$. The semi-amplitudes are $K_1 = 10.672 \pm 0.044$ km s $^{-1}$ and $K_2 = 13.551 \pm 0.226$ km s $^{-1}$, which gives the mass ratio of $q = M_2/M_1 = K_1/K_2 = 0.788 \pm 0.013$. The systemic velocity is $\gamma = -50.954 \pm 0.021$ km s $^{-1}$. All HPF spectra for this system were obtained in the ‘pre’ era, so only a single systemic velocity is required to describe the measurements.

The minimum masses from the RV orbit analysis are $M_1 \sin^3 i = 0.058 \pm 0.002 M_{\odot}$ and $M_2 \sin^3 i = 0.046 \pm 0.001 M_{\odot}$. The posterior distributions for LSPM J0515+5911 are included in Figure 9. If these minimum masses were close to the true mass (i.e., if i is close to 90°), then both components would be sub-stellar brown dwarfs. This is implausible because the spectra of such objects would not be well represented by our HPF-Specmatch templates. Were the true mass of these objects in the L dwarf regime, the resulting correlation values would have been very small because the spectral lines would not be a good match. Using the SED fit procedure in §3.2, we estimate the primary star’s mass to be $0.104_{-0.003}^{+0.006} M_{\odot}$ and age to be $9.3_{-4.1}^{+2.9}$ Gyrs. LSPM J0515+5911 must therefore be on an inclined orbit with an inclination of $i \sim 48^\circ$ required to match the predicted stellar mass, which clearly excludes the possibility of eclipses. This primary mass estimate, when combined with our measurement of q , gives a secondary mass of $M_2 \sim 0.08 \pm 0.01 M_{\odot}$, which is consistent with the temperature of stellar template we used for the cross-correlation analysis.

4.2. NLTT 45468

NLTT 45468 is an M4 type star in a binary system with a period of 9.686 ± 0.001 days. The nearby star shown in Figure 1b at a distance of $\sim 2''$ is close enough to cause some contamination in the $1.7''$ HPF fiber, but the effect is difficult to quantify when combined with variable seeing and guiding over years of observations. This object is resolved in Gaia (Gaia DR3 1435275918821040000) with a parallax of 34.56 mas, nearly identical to NLTT 45468, and a $\Delta G_{\text{mag}} \sim 2$, which suggestss that this is likely a bound wide companion, with a velocity close to the systemic velocity of the short period system. To assess the potential impact on our RV measurements, we analyzed the HPF spectra of NLTT 45468 using HPF-SERVAL (Stefansson et al. 2020; Stefánsson et al. 2023), which provides measurements of the differential line width, δLW , which is the second moment of the cross-correlation function (Zechmeister et al. 2018). Variations in δLW are attributable

⁶ <https://github.com/jvines/astroARIADNE>

Table 3. Model Priors and Derived Stellar Parameters for the Spectroscopic Binaries

Parameter	LSPM J0515+5911	NLTT 45468	NLTT 43564
Priors			
Orbital Parameters:			
P (days)	$\mathcal{N}(126.91, 1)$	$\mathcal{N}(9.69, 1)$	$\mathcal{N}(1888.04, 25)$
T_0 (BJD _{TDB})	$\mathcal{N}(2459080.8, 1)$	$\mathcal{N}(2458739.5, 1)$	$\mathcal{N}(2459662.6, 1)$
K_1 (km s ⁻¹)	$\mathcal{U}(0, 15)$	$\mathcal{U}(0.1, 0.3)$	$\mathcal{U}(0, 1)$
$\log(K_2)$ (km s ⁻¹)	$\mathcal{U}(0, 2.708)$
$\sqrt{e} \cos \omega$	$\mathcal{U}(-1, 1)$	$\mathcal{U}(-1, 1)$	$\mathcal{U}(-1, 1)$
$\sqrt{e} \sin \omega$	$\mathcal{U}(-1, 1)$	$\mathcal{U}(-1, 1)$	$\mathcal{U}(-1, 1)$
Jitter and Instrumental Terms:			
$\log(\sigma_{RV1})$	$\mathcal{N}(0, 1)$	$\mathcal{N}(0, 1)$	$\mathcal{N}(0, 1)$
$\log(\sigma_{RV2})$	$\mathcal{N}(0, 1)$
$\gamma_{\text{pre-HPF}}$ (km s ⁻¹)	$\mathcal{N}(0, 100)$	$\mathcal{N}(0, 100)$	$\mathcal{N}(0, 100)$
$\gamma_{\text{post-HPF}}$ (km s ⁻¹)	...	$\mathcal{N}(0, 100)$	$\mathcal{N}(0, 100)$
Derived Parameters			
Orbital Parameters:			
P (days)	126.948 ± 0.029	9.686 ± 0.001	1876.750 ± 23.634
T_0 (BJD _{TDB})	2459081.322 ± 0.122	2458739.118 ± 0.321	2459662.762 ± 0.945
K_1 (km s ⁻¹)	10.672 ± 0.044	0.167 ± 0.013	0.823 ± 0.022
K_2 (km s ⁻¹)	13.551 ± 0.226
ω (radians)	-2.758 ± 0.006	-0.246 ± 0.242	1.261 ± 0.029
$\sqrt{e} \cos \omega$	-0.529 ± 0.002	0.243 ± 0.069	0.208 ± 0.018
$\sqrt{e} \sin \omega$	-0.213 ± 0.003	-0.061 ± 0.055	0.648 ± 0.012
e	0.571 ± 0.002	0.257 ± 0.068	0.681 ± 0.009
Other Parameters:			
q	0.788 ± 0.013
$M_1 \sin^3 i(M_\odot)$	0.058 ± 0.002
$M_2 \sin^3 i(M_\odot)$	0.046 ± 0.001
$a_1 \sin i(AU)$	0.1022 ± 0.0004	0.000144 ± 0.000009	0.1040 ± 0.0039
$a_2 \sin i(AU)$	0.1298 ± 0.0021
$f(M_\odot)$	$(4.0 \pm 0.38) \times 10^{-5}$	$(4.0 \pm 1.0) \times 10^{-9}$	$(8.85 \pm 0.12) \times 10^{-3}$
Jitter and Instrumental Terms:			
$\log(\sigma_{RV1(Pre-HPF)})$	-2.820 ± 0.351	-3.657 ± 0.400	-3.897 ± 0.383
$\log(\sigma_{RV1(Post-HPF)})$...	-3.954 ± 0.369	-4.168 ± 0.378
$\log(\sigma_{RV2})$ (km s ⁻¹)	-1.266 ± 0.561
$\gamma_{\text{pre-HPF}}$ (km s ⁻¹)	-50.954 ± 0.021	-11.996 ± 0.013	-32.689 ± 0.016
$\gamma_{\text{post-HPF}}$ (km s ⁻¹)	...	-12.002 ± 0.008	-32.734 ± 0.015
Primary Star Parameters^b:			
T_{eff} (K)	2875 ± 59	3137 ± 59	3322 ± 59
$\log g$	5.17 ± 0.04	5.01 ± 0.04	4.94 ± 0.04
$[Fe/H]$	-0.02 ± 0.16	-0.06 ± 0.16	-0.15 ± 0.16
Mass (M_\odot)	$0.104^{+0.006}_{-0.003}$	$0.35^{+0.02}_{-0.07}$	0.32 ± 0.02
Age (Gyr)	$9.3^{+2.9}_{-4.1}$	$0.36^{+12.22}_{-0.36}$	$2.68^{+10.04}_{-1.62}$

^a Model priors follow $\mathcal{N}(\mu, \sigma)$ for normal and $\mathcal{U}(a, b)$ for uniform distributions.

^b The stellar parameters are derived with **HPF-SpecMatch** (T_{eff} , $\log g$, $[Fe/H]$) or SED fitting and stellar evolution models (mass and age).

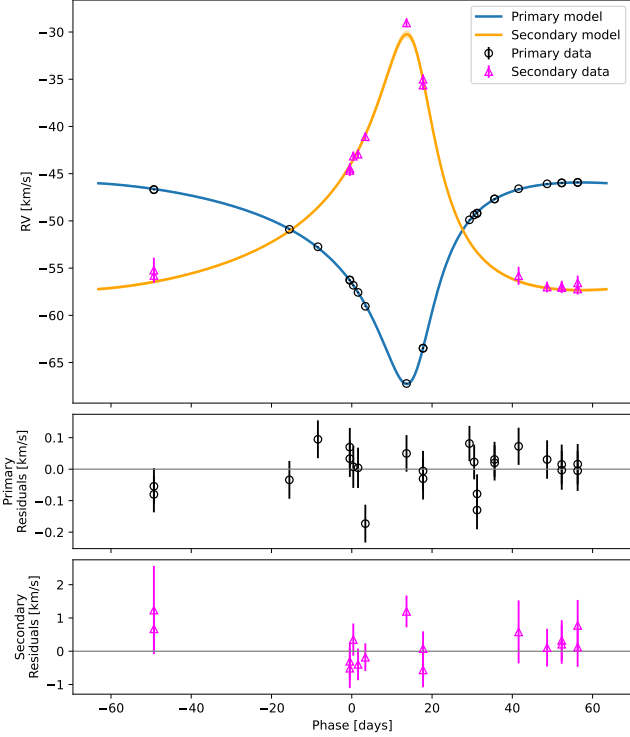


Figure 4. Radial velocity vs orbital phase for LSPM J0515+5911. Upper Panel: open black circles and open magenta triangles show our HPF primary and secondary velocities, respectively. The solid lines show the best orbital solution from Table 3. Lower Panels: Observed — calculated residuals for the primary and secondary velocities.

to variations in the shape of the spectral lines, often due to stellar activity, but also possibly due to a nearby star whose contamination level varies between observations. Figure 5 shows a strong correlation between δLW and the RVs, suggesting that there is indeed contamination from the companion affecting the correlations. This contamination will manifest as a weak correlation signal at a velocity near the primary overlapping which would reduce the signal to noise of the secondary and potentially cause a bias in the velocity measured of the secondary star if we were able to do so.

We solved NLTT 45468 as a single lined spectroscopic binary; no secondary component was evident in our **SXCORR** analysis. We used **HPF-Specmatch** to derive the stellar parameters to be $T_{eff} = 3127 \pm 59$ K, $\log g = 5.03 \pm 0.04$, and $[M/H] = -0.05 \pm 0.16$, $v \sin i = 4 \pm 1$ km s $^{-1}$, and used a template constructed from an HPF spectrum of GJ 9066. The eccentricity of the SB1 orbit is $e = 0.2571 \pm 0.068$. The semi-amplitude is $K_1 = 0.167 \pm 0.013$ km s $^{-1}$. The systemic velocities for the pre and post HPF eras are $\gamma_{preHPF} = -11.996 \pm 0.013$ km s $^{-1}$ and $\gamma_{postHPF} = -12.002 \pm 0.008$ km s $^{-1}$, respectively. The minimum value of the semi-major axis of the

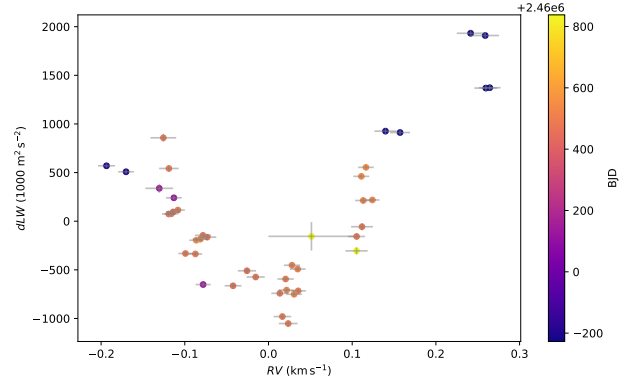


Figure 5. Differential line width (δLW) vs. RV for NLTT 45468. The significant change in δLW suggests contamination in the spectra, possibly from the nearby star at 2''.

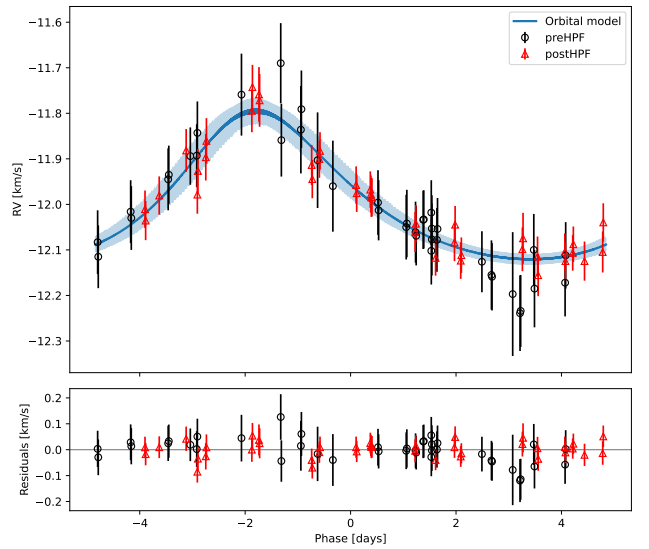


Figure 6. RV vs orbital phase for NLTT 45468. *Upper Panel:* Open black circles and open red triangles show primary HPF V_{pre} and V_{post} , respectively, corrected for the relative offset to be on the plotted on the same plot. The solid lines show the best orbital solution (Table 3). *Lower Panels:* Observed - calculated residuals for the HPF pre and post primary RVs

primary star's orbit is $a_1 \sin i = 0.031 \pm 0.002 R_{\odot}$. The posterior distributions for NLTT 45468 are included in Appendix A, Figure 11. From the SED fit, we estimate the primary star's mass to be $0.35^{+0.02}_{-0.06} M_{\odot}$ and age to be $0.36^{+12.22}_{-0.36}$ Gyrs.

The relatively short 9.7 day orbital period of NLTT 45468 opens the possibility for a geometric alignment that would cause eclipses. We analyzed the light curves from TESS-SPOC with 41 sectors of data, adapting the procedure used in [Stefánsson et al. \(2023\)](#). Our analysis included processing of data by doing a sigma clipping,

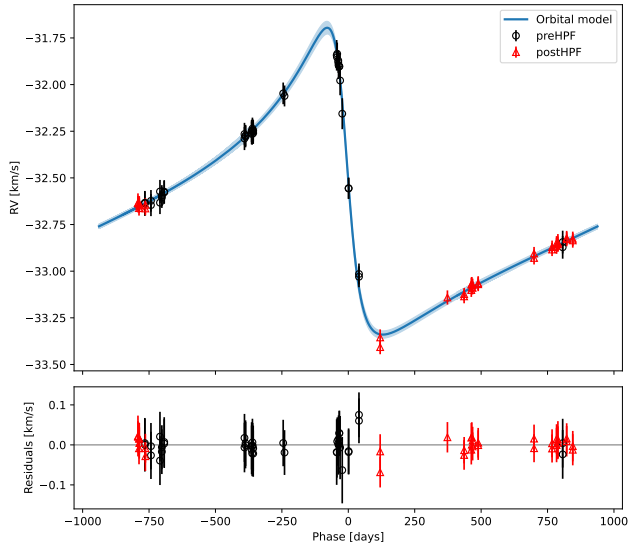


Figure 7. Same as Figure 6, but for NLTT 43564.

with upper bound = 3 and lower bound = 5. We then detrended the light curves using Wotan⁷ (Hippke et al. 2019) keeping the window length = 0.50 and then performed a transit least squares (TLS)⁸ search (Hippke & Heller 2019). We adopted the recommended signal detection efficiency threshold of 7 (corresponding to a 1% false positive rate) with TLS. Due to the difference in noise properties across sectors, we performed this analysis for each individual sector of data. We did not find any significant and consistent transit events in any of the 41 sectors.

This low-mass binary presents an interesting opportunity for followup observations at higher angular and spectral resolution. An adaptive optics fed spectrograph optimized for the near-infrared, such as iLocater (Crass et al. 2022) on the Large Binocular Telescope, could easily eliminate the signal from the wide companion that contaminates HPF spectra, and at the same time apply higher-spectral resolution to reduce blending in velocity space between the short period objects. Alternatively, a seeing limited spectrograph with a smaller diameter fiber, such as NEID on WIYN telescope, with $R \sim 115,000$, may also be able to detect a signal from the secondary.

4.3. NLTT 43564

NLTT 43564 is an M4 type star in a highly eccentric binary system with a period of 1870 ± 24 days. We solved NLTT 43564 as a single-lined spectroscopic binary; no

secondary component was evident in our SXCorr analysis. We used HPF-Specmatch to derive the stellar parameters of the primary star to be: $T_{eff} = 3322 \pm 59$ K, $\log g = 4.94 \pm 0.04$, and $[M/H] = -0.15 \pm 0.16$, $v \sin i = 1.4 \pm 0.4$ km s $^{-1}$ and used a template constructed from an HPF spectrum of GJ 105. Figure 7 shows the phased velocities and our derived orbital solution. Because of the very long orbital period, the phased plot is nearly identical to an unphased plot: the first observation occurs around +800 days, and the last observation occurs near -700 days, corresponding to a total span of just over one full orbit.

This system is highly eccentric: $e = 0.681 \pm 0.009$. The semi-amplitude is $K_1 = 0.823 \pm 0.022$ km s $^{-1}$. The systemic velocities pre and post HPF era are $\gamma_{preHPF} = -32.689 \pm 0.016$ km s $^{-1}$ and $\gamma_{postHPF} = -32.734 \pm 0.015$ km s $^{-1}$, consistent to within the 1σ uncertainties. From the SED fit analysis, we estimate the primary star's mass to be $0.32 \pm 0.02 M_{\odot}$ and age to be $2.68^{+10.04}_{-1.62}$ Gyrs.

This system has a long orbital period, which opens the possibility of detecting astrometric motion that could be combined with RVs to derive a fully dynamical orbital solution. Gaia DR3 reports a large RUWE of 17.164, which is consistent with this system being a binary (Lindegren et al. 2018). Gaia DR4, which is anticipated in late 2026, should significantly improve on the astrometric precision achieved for binaries like NLTT 43564, and so could enable a more model independent analysis of the system's orbital parameters. However, to achieve a fully dynamical solution would still require detecting the companion spectroscopically. Such a measurement could be attempted by a targeted campaign with HPF or other RV spectrograph for very high-S/N spectra near binary quadrature.

4.4. Additional analyses

To better understand the properties of the three binary systems we have presented here in the context of other solar neighborhood systems, we have plotted them in Figure 8 their blended light colors as seen by Gaia on a color-magnitude diagram generated from Gaia DR3 measurements of stars within 100 pc of the Sun (Gaia Collaboration et al. 2021). We also show the positions of the main sequence and the transition between partially and fully convective stellar interiors as parameterized by (Jao et al. 2023). All of our stars are cool, fully-convective, M dwarfs. NLTT 43564 lies close to the HR gap, which provides further motivation for future efforts to solve this system fully dynamically. LSPM J0515+5911 sits at a very interesting position at the bottom of the main-sequence, but its moderate inclination, medium period, and relative faintness combine to

⁷ <https://github.com/hippke/wotan>

⁸ <https://github.com/hippke/tls>

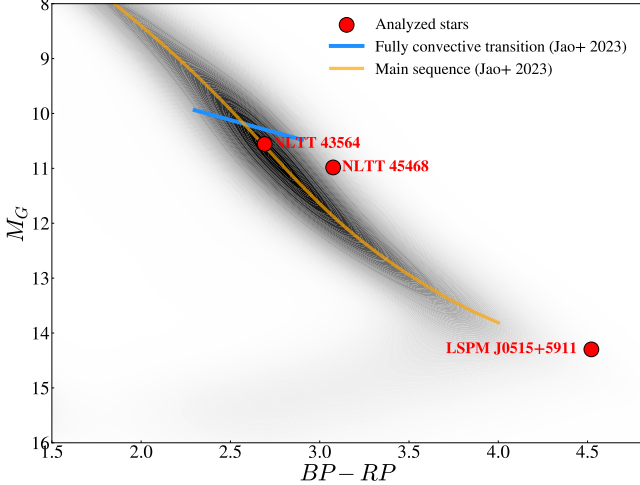


Figure 8. Color-magnitude diagram for nearby stars (within 100 pc) showing the local main sequence in M_G vs $BP - RP$. The background density map is constructed from the Gaia Catalogue of Nearby Stars (Gaia Collaboration et al. 2021). The three analyzed binary star targets, LSPM J0515+5911, NLTT 45468, and NLTT 43564, are plotted as red markers and they include light from the unresolved companion as seen by Gaia. The blue line indicates the observational transition to fully convective M dwarfs and the orange curve shows the empirical main-sequence points from Jao et al. (2023).

make followup observations that could solve this system fully dynamically quite challenging.

For single-lined binaries where we are unable to detect a signal from the secondary component in our spectra, we can estimate an upper limit on the secondary mass by considering the excess astrometric noise, ϵ , measured by Gaia, attributed to an offset between the center of light and the center of mass due to Keplerian orbital motion (Penoyre et al. 2020). For NLTT 45468, the simplification where the orbital period is much less than the observing window of Gaia Penoyre et al. (2020) Eq. 17 applies. In the limit where the secondary is “dark”, which is consistent with our lack of detection in the HPF spectra, we can set the luminosity ratio $l = L_2/L_1 = 0$. Following the parameterization in (Cañas et al. 2022, Eq. 2), with $\epsilon \sim 0.09208$ mas and the orbital parameters in Table 3, we estimate an upper limit on the secondary mass for NLTT 45468 of $M_2 = 0.016 M_\odot$, suggesting that the companion is substellar. If we consider an upper limit of $l = 0.05$, which would easily be detectable in our HPF spectra, the upper limit is $M_2 = 0.035 M_\odot$, which is still quite securely sub-stellar. For NLTT 43564, the long orbital period means that the full solution for long period binaries in Penoyre et al. (2020, Appendix B) must be used. We used the Gaia

Observation Forecast Tool⁹ to estimate the dates that Gaia observed NLTT 43564 during the time period represented by DR3. With $\epsilon = 2.822$ mas, and making the same $l = 0.0$ limit as above, we estimate an upper limit on $M_2 = 0.022 M_\odot$. In the upper limit of $l = 0.05$, we estimate $M_2 = 0.035 M_\odot$. For both of these binaries, the Gaia excess astrometric noise suggests that the secondary objects are substellar. This further motivates the future work suggested in §4.2 and §4.3 to push for additional dynamical constraints on these systems.

The age in all of our M dwarf targets are weakly constrained. However, the rotational properties of low-mass stars provide a useful diagnostic. As M dwarfs evolve, they gradually lose angular momentum through magnetic braking, causing their rotation periods to increase over time (Engle & Guinan 2011). This spin-down behavior enables age estimation via gyrochronology (Barnes 2003; Kiraga & Stepien 2007; Guinan et al. 2016; Popinchalk et al. 2021). For early-type M dwarfs (M0–M1 V), Engle & Guinan (2023) derived an empirical relation connecting rotation period to stellar age. However, in the mass regime for the stars presented here, this relationship is complicated (e.g., Newton et al. 2016; Engle & Guinan 2023; Gaidos et al. 2023). All three systems lie in the regime in the color-magnitude diagrams in Popinchalk et al. (2021) of G vs $G - G_{RP}$ that correspond to field star populations with unmeasured rotational velocities. Reliably measuring these from our HPF spectra at $R \sim 53,000$ would be extremely difficult. This is consistent with the ages we report in Table 3, which are extremely uncertain, but consistent with main-sequence stars.

5. SUMMARY

We used ground-based observations from HPF, NESSI, ’Alopeke, and Robo-AO, to derive the orbital parameters and constrain the stellar components of three spectroscopic binary systems comprised of fully-convective stars: LSPM J0515+5911, NLTT 45468, and NLTT 43564. LSPM J0515+5911 and NLTT 43564 are particularly interesting because their orbital periods are sufficiently long to suggest that the individual components are not tidally interacting, and so evolved as single stars. We solved LSPM J0515+5911 as an SB2 and determined that it is comprised of two late-type M dwarf stars in an eccentric orbit, with masses of $M_1 = 0.104 \pm 0.01 M_\odot$ and $M_2 = 0.08 \pm 0.01 M_\odot$. We solved NLTT 43564 and NLTT 45468 as SB1s, and estimate the primary masses to be $M_1 \sim 0.35 M_\odot$ and

⁹ <https://gaia.esac.esa.int/gost/index.jsp>

$M_1 \sim 0.32 M_{\odot}$, respectively. Each of these masses are consistent with the stellar temperatures that we derived from our HPF spectral template analyses. NLTT 45468 has a nearby companion that contaminates our seeing-limited HPF spectra, making it an ideal candidate for followup observations with an AO spectrograph such as iLocater. NLTT 43564 has a period of more than 5 years, and is a promising candidate for a full astrometric + spectroscopic analysis upon the release of Gaia DR4.

These binaries are part of a large observational program using HPF to followup eclipsing and non-eclipsing low-mass binary stars. Most of these targets were originally included in programs searching for exoplanets around M dwarfs. We have continued observing them, even after the signature of a stellar companion was detected, because of the utility of dynamical measurements of low-mass stellar binaries. Some targets that we continue to monitor, and plan to publish in future papers, have periods even longer than NLTT 43564, and so are prime candidates for combining results from spectroscopy and astrometry to yield fully dynamical solutions.

CIC acknowledges support from NASA Headquarters (i) through an appointment to the NASA Postdoctoral Program at the Goddard Space Flight Center, administered by ORAU through a contract with NASA and (ii) under award number 80GSFC24M0006.

Resources supporting this work were provided by the Pennsylvania State University's Institute for Computational and Data Sciences' (ICDS) Roar supercomputer. This content is solely the responsibility of the authors and does not represent the views of ICDS.

We acknowledge support from NSF grants AST 1006676, AST 1126413, AST 1310875, AST 1310885, AST 2009554, AST 2009889, AST 2108512, AST 2108801 and the NASA Astrobiology Institute (NNA09DA76A) in our pursuit of precision RVs in the near-infrared. We acknowledge the support of the Heising-Simons Foundation through grant 2017-0494. These results are based on observations obtained with HPF on the HET. The HET is a joint project of the University of Texas at Austin, the Pennsylvania State University, Ludwig-Maximilians-Universität München, and Georg-August Universität Gottingen. The HET is named in honor of its principal benefactors, William P. Hobby and Robert E. Eberly. The HET collaboration acknowledges the support and resources from the Texas Advanced Computing Center. We are grateful to the HET Resident Astronomers and Telescope Operators for their valuable assistance in gathering our HPF data. We would like to acknowledge that the HET is built on Indigenous land. Moreover, we would like to acknowledge and pay our respects to the Carrizo & Comecrudo, Coahuiltecan, Caddo, Tonkawa, Comanche, Lipan Apache, Alabama-Coushatta, Kickapoo, Tigua Pueblo, and all the American Indian and Indigenous Peoples and communities who have been or have become a part of these lands and territories in Texas, here on Turtle Island.

Some of the observations were obtained at the WIYN Observatory from telescope time allocated to NN-EXPLORE (PI: Gupta; 2022A-665981) through the scientific partnership of NASA, the NSF, and NOIRLab. These observations used the NN-EXPLORE Exoplanet and Stellar Speckle Imager (NESSI). NESSI was funded by the NASA Exoplanet Exploration Program and the NASA Ames Research Center. NESSI was built at the Ames Research Center by Steve B. Howell, Nic Scott, Elliott P. Horch, and Emmett Quigley. WIYN is a joint facility of the University of Wisconsin-Madison, Indiana University, NSF's NOIRLab, the Pennsylvania State University, Purdue University, the University of California-Irvine, and the University of Missouri. The authors are honored to be permitted to conduct astronomical research on Iolkam Du'ag (Kitt Peak), a mountain with particular significance to the Tohono O'odham.

Some of the data presented in this paper were obtained from MAST at STScI. Support for MAST for non-HST data is provided by the NASA Office of Space Science via grant NNX09AF08G and by other grants and contracts. This work includes data collected by the TESS mission, which are publicly available from MAST. Funding for the TESS mission is provided by the NASA Science Mission directorate. This research made use of the (i) NASA Exoplanet Archive, which is operated by Caltech, under contract with NASA under the Exoplanet Exploration Program, (ii) SIMBAD database, operated at CDS, Strasbourg, France, (iii) NASA’s Astrophysics Data System Bibliographic Services, (iv) NASA/IPAC Infrared Science Archive, which is funded by NASA and operated by the California Institute of Technology, and (v) data from 2MASS, a joint project of the University of Massachusetts and IPAC at Caltech, funded by NASA and the NSF.

This work has used data from the European Space Agency (ESA) mission Gaia (<https://www.cosmos.esa.int/Gaia>), processed by the Gaia Data Processing and Analysis Consortium (DPAC, <https://www.cosmos.esa.int/web/Gaia/dpac/consortium>). Funding for the DPAC has been provided by national institutions, in particular the institutions participating in the Gaia Multilateral Agreement.

Facilities: TESS, RBO, WIYN (NESSI), HET (HPF), Gemini:Gillett ('Alopeke), Robo-AO, MAST

Software: Astropy ([Astropy Collaboration et al. 2013, 2018, 2022](#)), HPF-SERVAL ([Stefansson 2023](#)), lightkurve ([Lightkurve Collaboration et al. 2018](#)), Matplotlib ([Hunter 2007](#)), NumPy ([van der Walt et al. 2011](#)), pandas ([McKinney 2010](#)), SciPy ([Oliphant 2007; Millman & Avazis 2011](#)), HPF-Specmatch ([Stefansson et al. 2020](#)), PyMC3 ([Salvatier et al. 2015](#)), exoplanet ([Foreman-Mackey et al. 2021](#)), astroARIADNE ([Vines & Jenkins 2022](#)), tls ([Hippke & Heller 2019](#))

APPENDIX

A. ADDITIONAL ANALYSIS

These corner plots summarize the posterior distributions obtained from our exoplanet modeling described above. We include them for completeness here.

REFERENCES

AER. 2020, AER Line File Parameters, 3.8.1, Zenodo, doi: [10.5281/zenodo.5120012](https://doi.org/10.5281/zenodo.5120012)

Alonso-Floriano, F. J., Morales, J. C., Caballero, J. A., et al. 2015, *A&A*, 577, A128, doi: [10.1051/0004-6361/201525803](https://doi.org/10.1051/0004-6361/201525803)

Astropy Collaboration, Robitaille, T. P., Tollerud, E. J., et al. 2013, *A&A*, 558, A33, doi: [10.1051/0004-6361/201322068](https://doi.org/10.1051/0004-6361/201322068)

Astropy Collaboration, Price-Whelan, A. M., Sipőcz, B. M., et al. 2018, *AJ*, 156, 123, doi: [10.3847/1538-3881/aabc4f](https://doi.org/10.3847/1538-3881/aabc4f)

Astropy Collaboration, Price-Whelan, A. M., Lim, P. L., et al. 2022, *ApJ*, 935, 167, doi: [10.3847/1538-4357/ac7c74](https://doi.org/10.3847/1538-4357/ac7c74)

Bailer-Jones, C. A. L., Rybizki, J., Fouesneau, M., Demleitner, M., & Andrae, R. 2021, *AJ*, 161, 147, doi: [10.3847/1538-3881/abd806](https://doi.org/10.3847/1538-3881/abd806)

Barnes, S. A. 2003, *ApJ*, 586, 464, doi: [10.1086/367639](https://doi.org/10.1086/367639)

Beard, C., Robertson, P., Lubin, J., et al. 2025, *AJ*, 170, 279, doi: [10.3847/1538-3881/ae0e20](https://doi.org/10.3847/1538-3881/ae0e20)

Bender, C. F., & Simon, M. 2008, *ApJ*, 689, 416, doi: [10.1086/592728](https://doi.org/10.1086/592728)

Bender, C. F., Mahadevan, S., Deshpande, R., et al. 2012, *ApJL*, 751, L31, doi: [10.1088/2041-8205/751/2/L31](https://doi.org/10.1088/2041-8205/751/2/L31)

Cañas, C. I., Mahadevan, S., Bender, C. F., et al. 2022, *AJ*, 163, 89, doi: [10.3847/1538-3881/ac415f](https://doi.org/10.3847/1538-3881/ac415f)

Chambers, K. C., Magnier, E. A., Metcalfe, N., et al. 2016, arXiv e-prints, arXiv:1612.05560, doi: [10.48550/arXiv.1612.05560](https://doi.org/10.48550/arXiv.1612.05560)

Christiansen, J. L., McElroy, D. L., Harbut, M., et al. 2025, *The Planetary Science Journal*, 6, 186, doi: [10.3847/PSJ/ade3c2](https://doi.org/10.3847/PSJ/ade3c2)

Clough, S. A., Iacono, M. J., & Moncet, J.-L. 1992, *J. Geophys. Res.*, 97, 15,761, doi: [10.1029/92JD01419](https://doi.org/10.1029/92JD01419)

Clough, S. A., Shephard, M. W., Mlawer, E. J., et al. 2005, *JQSRT*, 91, 233, doi: [10.1016/j.jqsrt.2004.05.058](https://doi.org/10.1016/j.jqsrt.2004.05.058)

Crass, J., Aikens, D., Mason, J., et al. 2022, in *Society of Photo-Optical Instrumentation Engineers (SPIE) Conference Series*, Vol. 12184, *Ground-based and Airborne Instrumentation for Astronomy IX*, ed. C. J. Evans, J. J. Bryant, & K. Motohara, 121841P, doi: [10.1117/12.2630228](https://doi.org/10.1117/12.2630228)

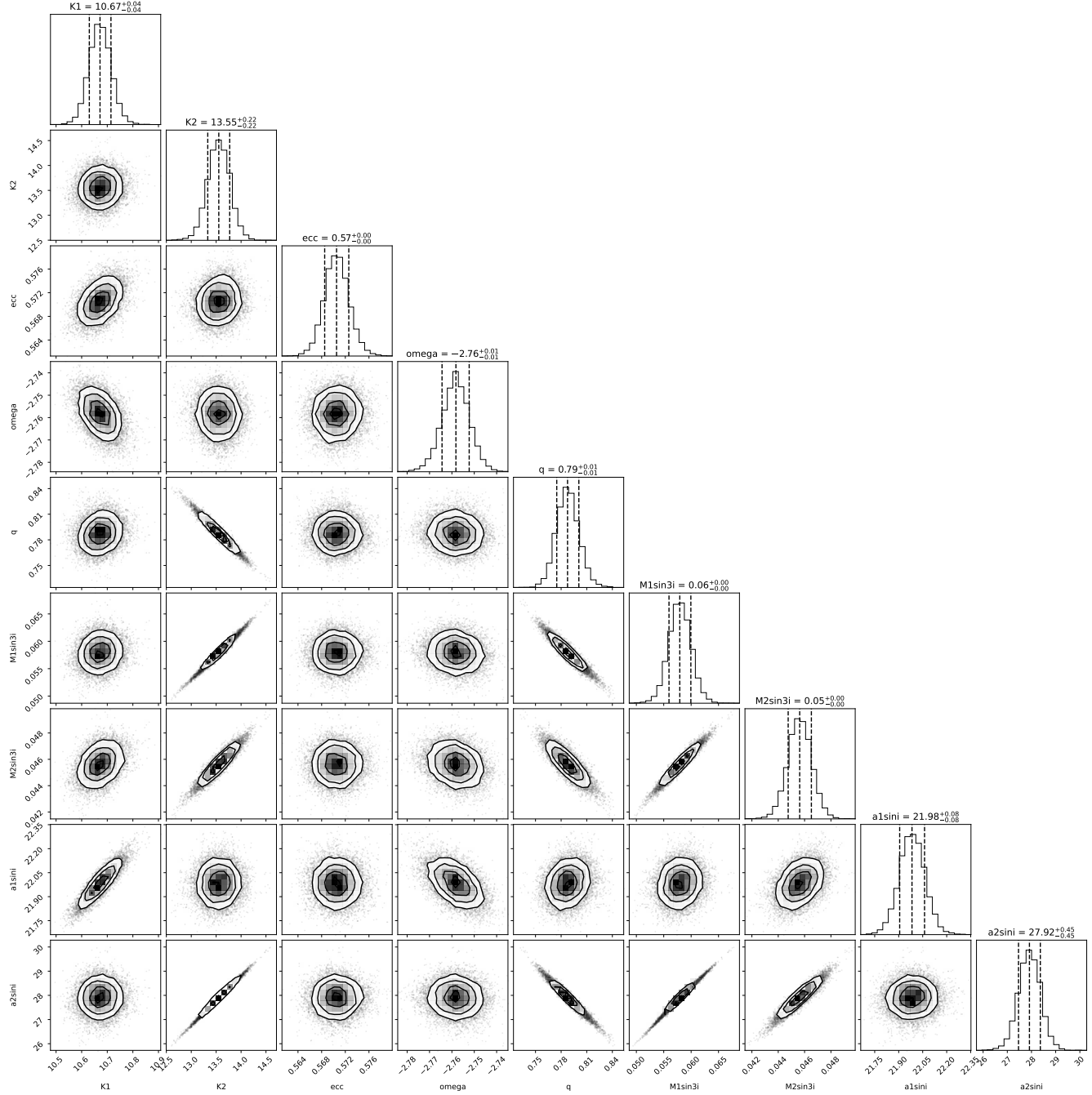


Figure 9. Posterior distributions obtained for LSPM J0515+5911, which was solved as a double-lined binary.

Cutri, R. M., Skrutskie, M. F., van Dyk, S., et al. 2003,

VizieR Online Data Catalog: 2MASS All-Sky Catalog of Point Sources (Cutri+ 2003), VizieR On-line Data Catalog: II/246. Originally published in: University of Massachusetts and Infrared Processing and Analysis Center, (IPAC/California Institute of Technology) (2003)

Cutri, R. M., Wright, E. L., Conrow, T., et al. 2021, VizieR

Online Data Catalog: AllWISE Data Release (Cutri+ 2013), VizieR On-line Data Catalog: II/328. Originally published in: IPAC/Caltech (2013)

Duquennoy, A., & Mayor, M. 1991, A&A, 248, 485

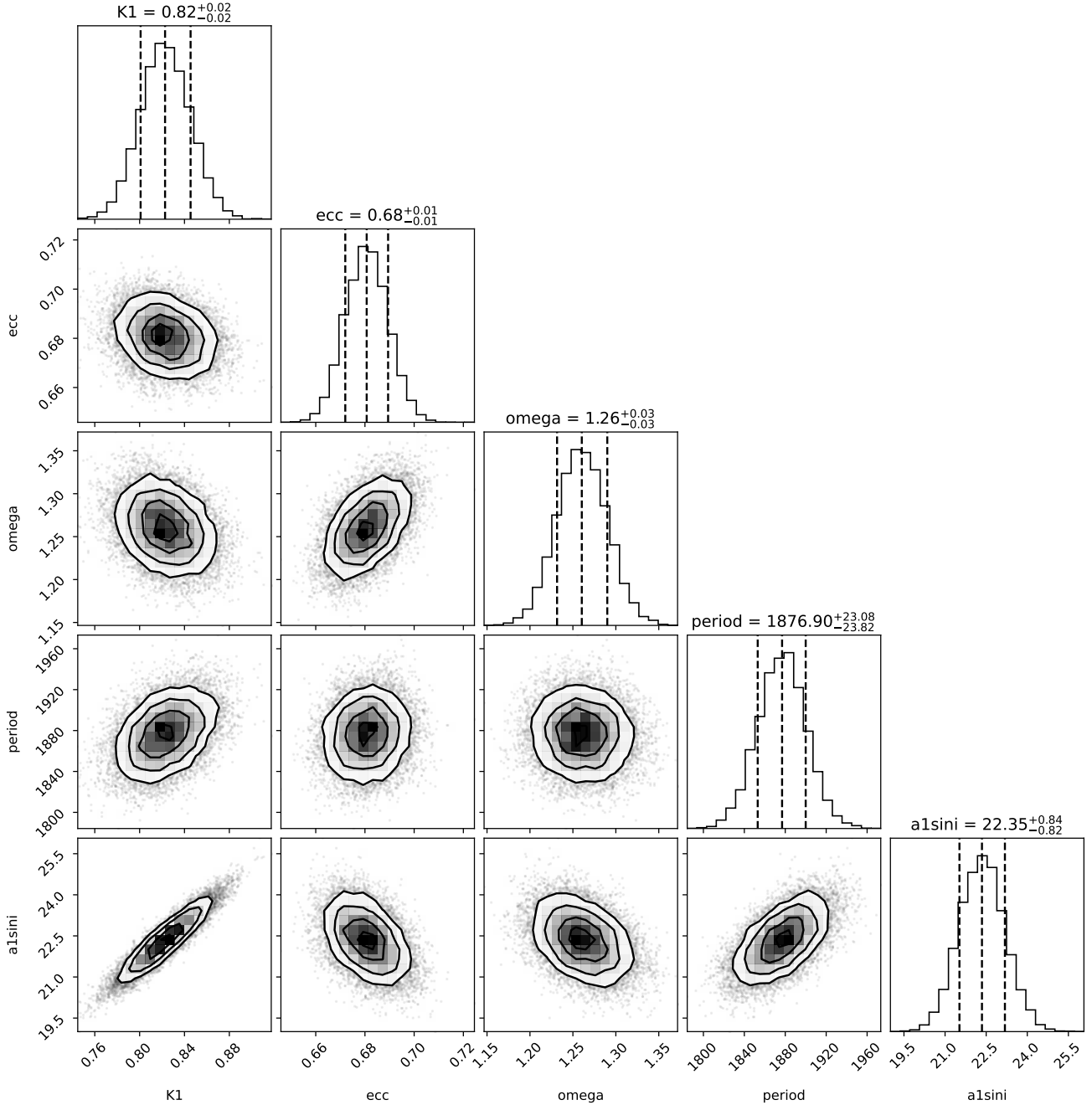


Figure 10. Posterior distributions obtained for NLTT 43564, which was solved as a single lined binary.

Engle, S. G., & Guinan, E. F. 2011, in Astronomical Society of the Pacific Conference Series, Vol. 451, 9th Pacific Rim Conference on Stellar Astrophysics, ed. S. Qain, K. Leung, L. Zhu, & S. Kwok, 285, doi: [10.48550/arXiv.1111.2872](https://arxiv.org/abs/1111.2872)

Engle, S. G., & Guinan, E. F. 2023, ApJL, 954, L50, doi: [10.3847/2041-8213/acf472](https://doi.org/10.3847/2041-8213/acf472)

Fitzpatrick, E. L. 1999, PASP, 111, 63, doi: [10.1086/316293](https://doi.org/10.1086/316293)

Fleming, S. W., Mahadevan, S., Deshpande, R., et al. 2015, AJ, 149, 143, doi: [10.1088/0004-6256/149/4/143](https://doi.org/10.1088/0004-6256/149/4/143)

Ford, E. B. 2006, ApJ, 642, 505, doi: [10.1086/500802](https://doi.org/10.1086/500802)

Foreman-Mackey, D., Luger, R., Agol, E., et al. 2021, The Journal of Open Source Software, 6, 3285, doi: [10.21105/joss.03285](https://doi.org/10.21105/joss.03285)

Gaia Collaboration, Brown, A. G. A., Vallenari, A., et al. 2018, A&A, 616, A1, doi: [10.1051/0004-6361/201833051](https://doi.org/10.1051/0004-6361/201833051)

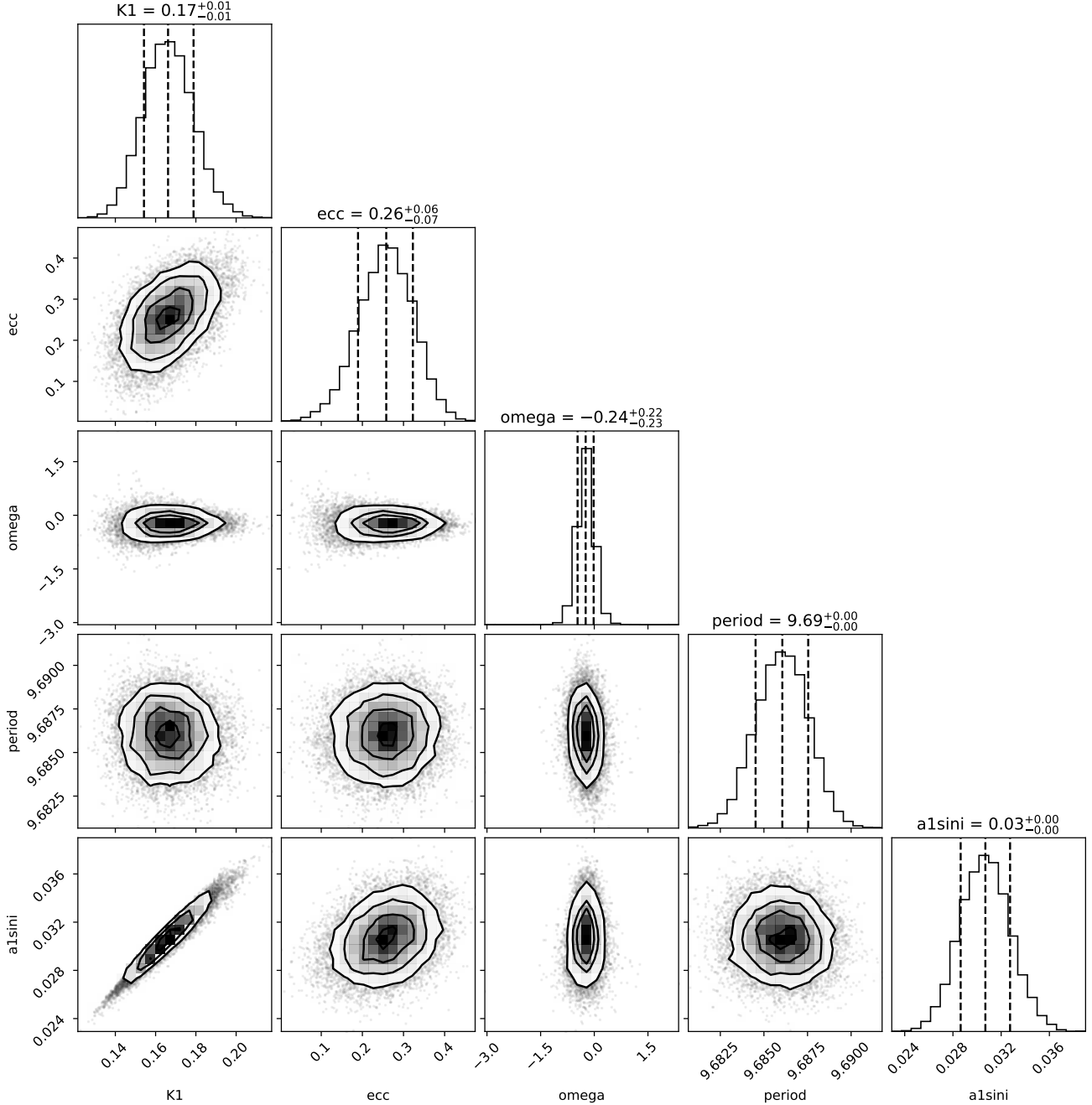


Figure 11. Posterior distributions obtained for NLTT 45468, which was solved as a single lined binary.

Gaia Collaboration, Smart, R. L., Sarro, L. M., et al. 2021,

A&A, 649, A6, doi: [10.1051/0004-6361/202039498](https://doi.org/10.1051/0004-6361/202039498)

Gaia Collaboration, Vallenari, A., Brown, A. G. A., et al. 2023, A&A, 674, A1, doi: [10.1051/0004-6361/202243940](https://doi.org/10.1051/0004-6361/202243940)

Gaidos, E., Claytor, Z., Dungee, R., Ali, A., & Feiden, G. A. 2023, MNRAS, 520, 5283, doi: [10.1093/mnras/stad343](https://doi.org/10.1093/mnras/stad343)

Gialluca, M. T., Robinson, T. D., Rugheimer, S., &

Wunderlich, F. 2021, PASP, 133, 054401, doi: [10.1088/1538-3873/abf367](https://doi.org/10.1088/1538-3873/abf367)

Gordon, I. E., Rothman, L. S., Hargreaves, R. J., et al. 2022, JQSRT, 277, 107949, doi: [10.1016/j.jqsrt.2021.107949](https://doi.org/10.1016/j.jqsrt.2021.107949)

Guinan, E. F., Engle, S. G., & Durbin, A. 2016, ApJ, 821, 81, doi: [10.3847/0004-637X/821/2/81](https://doi.org/10.3847/0004-637X/821/2/81)

Hardegree-Ullman, K. K., Apai, D., Bergsten, G. J., Pascucci, I., & López-Morales, M. 2023, AJ, 165, 267, doi: [10.3847/1538-3881/acd1ec](https://doi.org/10.3847/1538-3881/acd1ec)

Henden, A. A., Levine, S., Terrell, D., & Welch, D. L. 2015, in American Astronomical Society Meeting Abstracts, Vol. 225, American Astronomical Society Meeting Abstracts #225, 336.16

Henry, T. J., Jao, W.-C., Subasavage, J. P., et al. 2006, AJ, 132, 2360, doi: [10.1086/508233](https://doi.org/10.1086/508233)

Henry, T. J., Jao, W.-C., Winters, J. G., et al. 2018, AJ, 155, 265, doi: [10.3847/1538-3881/aac262](https://doi.org/10.3847/1538-3881/aac262)

Hill, G. J., Lee, H., MacQueen, P. J., et al. 2021, AJ, 162, 298, doi: [10.3847/1538-3881/ac2c02](https://doi.org/10.3847/1538-3881/ac2c02)

Hippke, M., David, T. J., Mulders, G. D., & Heller, R. 2019, AJ, 158, 143, doi: [10.3847/1538-3881/ab3984](https://doi.org/10.3847/1538-3881/ab3984)

Hippke, M., & Heller, R. 2019, A&A, 623, A39, doi: [10.1051/0004-6361/201834672](https://doi.org/10.1051/0004-6361/201834672)

Howell, S. B., Everett, M. E., Sherry, W., Horch, E., & Ciardi, D. R. 2011, AJ, 142, 19, doi: [10.1088/0004-6256/142/1/19](https://doi.org/10.1088/0004-6256/142/1/19)

Hunter, J. D. 2007, Computing in Science and Engineering, 9, 90, doi: [10.1109/MCSE.2007.55](https://doi.org/10.1109/MCSE.2007.55)

Jao, W.-C., Henry, T. J., White, R. J., et al. 2023, AJ, 166, 63, doi: [10.3847/1538-3881/ace2bb](https://doi.org/10.3847/1538-3881/ace2bb)

Kanodia, S., & Wright, J. T. 2018, Barycorpy: Barycentric velocity calculation and leap second management, Astrophysics Source Code Library, record ascl:1808.001

Kanodia, S., Mahadevan, S., Ramsey, L. W., et al. 2018, in Society of Photo-Optical Instrumentation Engineers (SPIE) Conference Series, Vol. 10702, Ground-based and Airborne Instrumentation for Astronomy VII, ed. C. J. Evans, L. Simard, & H. Takami, 107026Q, doi: [10.1117/12.2313491](https://doi.org/10.1117/12.2313491)

Kiraga, M., & Stepień, K. 2007, AcA, 57, 149, doi: [10.48550/arXiv.0707.2577](https://doi.org/10.48550/arXiv.0707.2577)

Kopparapu, R. k., Wolf, E. T., Arney, G., et al. 2017, ApJ, 845, 5, doi: [10.3847/1538-4357/aa7cf9](https://doi.org/10.3847/1538-4357/aa7cf9)

Kopparapu, R. K., Ramirez, R., Kasting, J. F., et al. 2013, ApJ, 765, 131, doi: [10.1088/0004-637X/765/2/131](https://doi.org/10.1088/0004-637X/765/2/131)

Lamman, C., Baranec, C., Berta-Thompson, Z. K., et al. 2020, AJ, 159, 139, doi: [10.3847/1538-3881/ab6ef1](https://doi.org/10.3847/1538-3881/ab6ef1)

Latouf, N., Wang, S. X., Cale, B., & Plavchan, P. 2022, AJ, 164, 212, doi: [10.3847/1538-3881/ac947b](https://doi.org/10.3847/1538-3881/ac947b)

Law, N. M., Morton, T., Baranec, C., et al. 2014, ApJ, 791, 35, doi: [10.1088/0004-637X/791/1/35](https://doi.org/10.1088/0004-637X/791/1/35)

Lépine, S., Rich, R. M., & Shara, M. M. 2003, AJ, 125, 1598, doi: [10.1086/345972](https://doi.org/10.1086/345972)

Lightkurve Collaboration, Cardoso, J. V. d. M., Hedges, C., et al. 2018, Lightkurve: Kepler and TESS time series analysis in Python, Astrophysics Source Code Library, <http://ascl.net/1812.013>

Lindegren, L., Hernández, J., Bombrun, A., et al. 2018, A&A, 616, A2, doi: [10.1051/0004-6361/201832727](https://doi.org/10.1051/0004-6361/201832727)

Lubin, J., Robertson, P., Stefansson, G., et al. 2021, VizieR Online Data Catalog: Radial velocity follow up of Barnard's star with HPF (Lubin+, 2021), VizieR On-line Data Catalog: J/AJ/162/61. Originally published in: 2021AJ....162...61L, doi: [10.26093/cds/vizier.51620061](https://doi.org/10.26093/cds/vizier.51620061)

Mahadevan, S., Ramsey, L., Bender, C., et al. 2012, in Society of Photo-Optical Instrumentation Engineers (SPIE) Conference Series, Vol. 8446, Ground-based and Airborne Instrumentation for Astronomy IV, ed. I. S. McLean, S. K. Ramsay, & H. Takami, 84461S, doi: [10.1117/12.926102](https://doi.org/10.1117/12.926102)

Mahadevan, S., Ramsey, L. W., Terrien, R., et al. 2014, in Society of Photo-Optical Instrumentation Engineers (SPIE) Conference Series, Vol. 9147, Ground-based and Airborne Instrumentation for Astronomy V, ed. S. K. Ramsay, I. S. McLean, & H. Takami, 91471G, doi: [10.1117/12.2056417](https://doi.org/10.1117/12.2056417)

Maxted, P. F. L., Triaud, A. H. M. J., & Martin, D. V. 2023, Universe, 9, 498, doi: [10.3390/universe9120498](https://doi.org/10.3390/universe9120498)

Mazeh, T., & Zucker, S. 1992, in Astronomical Society of the Pacific Conference Series, Vol. 32, IAU Colloquium 135: Complementary Approaches to Double and Multiple Star Research, ed. H. A. McAlister & W. I. Hartkopf, 164

McKinney, W. 2010, Proceedings of the 9th Python in Science Conference, 51

Metcalf, A. J., Anderson, T., Bender, C. F., et al. 2019, Optica, 6, 233, doi: [10.1364/OPTICA.6.000233](https://doi.org/10.1364/OPTICA.6.000233)

Millman, K. J., & Aivazis, M. 2011, Computing in Science and Engineering, 13, 9, doi: [10.1109/MCSE.2011.36](https://doi.org/10.1109/MCSE.2011.36)

Newton, E. R., Irwin, J., Charbonneau, D., et al. 2016, in 19th Cambridge Workshop on Cool Stars, Stellar Systems, and the Sun (CS19), Cambridge Workshop on Cool Stars, Stellar Systems, and the Sun, 4, doi: [10.5281/zenodo.153997](https://doi.org/10.5281/zenodo.153997)

NExSci. 2022, Exoplanet Follow-up Observing Program Web Service, IPAC, doi: [10.26134/EXOFOP5](https://doi.org/10.26134/EXOFOP5)

Ninan, J. P., Mahadevan, S., Stefansson, G., et al. 2019, Journal of Astronomical Telescopes, Instruments, and Systems, 5, 041511, doi: [10.1117/1.JATIS.5.4.041511](https://doi.org/10.1117/1.JATIS.5.4.041511)

Oliphant, T. E. 2007, Computing in Science and Engineering, 9, 10, doi: [10.1109/MCSE.2007.58](https://doi.org/10.1109/MCSE.2007.58)

Parsons, S. G., Gänsicke, B. T., Marsh, T. R., et al. 2018, MNRAS, 481, 1083, doi: [10.1093/mnras/sty2345](https://doi.org/10.1093/mnras/sty2345)

Penoyre, Z., Belokurov, V., Wyn Evans, N., Everall, A., & Koposov, S. E. 2020, MNRAS, 495, 321, doi: [10.1093/mnras/staa1148](https://doi.org/10.1093/mnras/staa1148)

Popinchalk, M., Faherty, J. K., Kiman, R., et al. 2021, ApJ, 916, 77, doi: [10.3847/1538-4357/ac0444](https://doi.org/10.3847/1538-4357/ac0444)

Raghavan, D., McAlister, H. A., Henry, T. J., et al. 2010, ApJS, 190, 1, doi: [10.1088/0067-0049/190/1/1](https://doi.org/10.1088/0067-0049/190/1/1)

Ramsey, L. W. 2005, in American Institute of Physics Conference Series, Vol. 752, Stellar Astrophysics with the World's Largest Telescopes, ed. J. Mikolajewska & A. Olech, 3–12, doi: [10.1063/1.1893326](https://doi.org/10.1063/1.1893326)

Ramsey, L. W., Adams, M. T., Barnes, T. G., et al. 1998, in Society of Photo-Optical Instrumentation Engineers (SPIE) Conference Series, Vol. 3352, Advanced Technology Optical/IR Telescopes VI, ed. L. M. Stepp, 34–42, doi: [10.1117/12.319287](https://doi.org/10.1117/12.319287)

Reid, I. N., Cruz, K. L., Allen, P., et al. 2004, AJ, 128, 463, doi: [10.1086/421374](https://doi.org/10.1086/421374)

Riddle, R. L., Burse, M. P., Law, N. M., et al. 2012, in Society of Photo-Optical Instrumentation Engineers (SPIE) Conference Series, Vol. 8447, Adaptive Optics Systems III, ed. B. L. Ellerbroek, E. Marchetti, & J.-P. Véran, 84472O, doi: [10.1117/12.925475](https://doi.org/10.1117/12.925475)

Salvatier, J., Wiecki, T., & Fonnesbeck, C. 2015, arXiv e-prints, arXiv:1507.08050, doi: [10.48550/arXiv.1507.08050](https://doi.org/10.48550/arXiv.1507.08050)

Schlafly, E. F., & Finkbeiner, D. P. 2011, ApJ, 737, 103, doi: [10.1088/0004-637X/737/2/103](https://doi.org/10.1088/0004-637X/737/2/103)

Schlegel, D. J., Finkbeiner, D. P., & Davis, M. 1998, ApJ, 500, 525, doi: [10.1086/305772](https://doi.org/10.1086/305772)

Scott, N. J., & Howell, S. B. 2018, in Optical and Infrared Interferometry and Imaging VI, ed. M. J. Creech-Eakman, P. G. Tuthill, & A. Mérand, Vol. 10701, International Society for Optics and Photonics (SPIE), 107010G, doi: [10.1117/12.2311539](https://doi.org/10.1117/12.2311539)

Scott, N. J., Howell, S. B., Horch, E. P., & Everett, M. E. 2018, PASP, 130, 054502, doi: [10.1088/1538-3873/aab484](https://doi.org/10.1088/1538-3873/aab484)

Shetrone, M., Cornell, M. E., Fowler, J. R., et al. 2007, PASP, 119, 556, doi: [10.1086/519291](https://doi.org/10.1086/519291)

Shields, A. L., Ballard, S., & Johnson, J. A. 2016, PhR, 663, 1, doi: [10.1016/j.physrep.2016.10.003](https://doi.org/10.1016/j.physrep.2016.10.003)

Spada, F., Demarque, P., Kim, Y.-C., & Sills, A. 2013, ApJ, 776, 87, doi: [10.1088/0004-637X/776/2/87](https://doi.org/10.1088/0004-637X/776/2/87)

Stefansson, G. 2023, gummiks/hpserval_lhs3154: HPF-SERVAL release for Stefansson et al. 2023., v1.0.0, Zenodo, doi: [10.5281/zenodo.8397170](https://doi.org/10.5281/zenodo.8397170)

Stefansson, G., Cañas, C., Wisniewski, J., et al. 2020, AJ, 159, 100, doi: [10.3847/1538-3881/ab5f15](https://doi.org/10.3847/1538-3881/ab5f15)

Stefansson, G., Cañas, C., Wisniewski, J., et al. 2020, The Astronomical Journal, 159, 100, doi: [10.3847/1538-3881/ab5f15](https://doi.org/10.3847/1538-3881/ab5f15)

Stefánsson, G., Mahadevan, S., Miguel, Y., et al. 2023, Science, 382, 1031, doi: [10.1126/science.abo0233](https://doi.org/10.1126/science.abo0233)

Stefánsson, G. K., Hearty, F. R., Robertson, P. M., et al. 2016, in Society of Photo-Optical Instrumentation Engineers (SPIE) Conference Series, Vol. 9908, Ground-based and Airborne Instrumentation for Astronomy VI, ed. C. J. Evans, L. Simard, & H. Takami, 990871, doi: [10.1117/12.2233443](https://doi.org/10.1117/12.2233443)

Tuchow, N., Stark, C., & Mamajek, E. 2024, arXiv e-prints, arXiv:2402.08038, doi: [10.48550/arXiv.2402.08038](https://doi.org/10.48550/arXiv.2402.08038)

van der Walt, S., Colbert, S. C., & Varoquaux, G. 2011, Computing in Science and Engineering, 13, 22, doi: [10.1109/MCSE.2011.37](https://doi.org/10.1109/MCSE.2011.37)

Vines, J. I., & Jenkins, J. S. 2022, MNRAS, doi: [10.1093/mnras/stac956](https://doi.org/10.1093/mnras/stac956)

Wright, J. T., & Eastman, J. D. 2014, Publications of the Astronomical Society of the Pacific, 126, 838–852, doi: [10.1086/678541](https://doi.org/10.1086/678541)

Yee, S. W., Petigura, E. A., & von Braun, K. 2017, ApJ, 836, 77, doi: [10.3847/1538-4357/836/1/77](https://doi.org/10.3847/1538-4357/836/1/77)

Zechmeister, M., Reiners, A., Amado, P. J., et al. 2018, A&A, 609, A12, doi: [10.1051/0004-6361/201731483](https://doi.org/10.1051/0004-6361/201731483)

Ziegler, C., Law, N. M., Baranec, C., et al. 2018, AJ, 155, 161, doi: [10.3847/1538-3881/aab042](https://doi.org/10.3847/1538-3881/aab042)

Zucker, S. 2003, MNRAS, 342, 1291, doi: [10.1046/j.1365-8711.2003.06633.x](https://doi.org/10.1046/j.1365-8711.2003.06633.x)